28. T. J. Drye, M. E. Cates, *J. Chem. Phys.* **96**, 1367 (1992).
29. P. Panizza, G. Cristobal, J. Curtly, *J. Phys. Cond. Matter* **10**, 11659 (1998).
30. A. Bernheim-Groswasser, E. Wachtel, Y. Talmon, *Langmuir* **16**, 4131 (2000).
31. T. Tlusty, S. A. Safran, *J. Phys. Cond. Matter* **12**, A253 (2000).
32. This research program was supported by the NSF-sponsored Materials Science and Engineering Center (MRSEC) at the University of Minnesota and by the NIH (1R21EB00989-01). D. Morse engaged the authors in enlightening discussions.

8 January 2003; accepted 11 March 2003

Multifunctional Alloys Obtained via a Dislocation-Free Plastic Deformation Mechanism

Takashi Saito,[1]* Tadahiko Furuta,[1] Jung-Hwan Hwang,[1] Shigeru Kuramoto,[1] Kazuaki Nishino,[1] Nobuaki Suzuki,[1] Rong Chen,[1] Akira Yamada,[1] Kazuhiko Ito,[1] Yoshiki Seno,[1] Takamasa Nonaka,[1] Hideaki Ikehata,[1] Naoyuki Nagasako,[1] Chihiro Iwamoto,[2] Yuuichi Ikuhara,[2] Taketo Sakuma[3]

We describe a group of alloys that exhibit "super" properties, such as ultralow elastic modulus, ultrahigh strength, super elasticity, and super plasticity, at room temperature and that show Elinvar and Invar behavior. These "super" properties are attributable to a dislocation-free plastic deformation mechanism. In cold-worked alloys, this mechanism forms elastic strain fields of hierarchical structure that range in size from the nanometer scale to several tens of micrometers. The resultant elastic strain energy leads to a number of enhanced material properties.

Mechanical properties, such as strength, of metallic materials are strongly affected by metallurgical processes such as heat treatment and plastic working, which bring modifications in the microstructure. On the other hand, these processes have no substantial effect on physical properties such as elastic modulus and thermal expansion. The reason for this is that the changes that can be affected by plastic working and heat treatment do not extend to interatomic bonds or electronic states.

We present a group of alloys that exhibit multiple "super" properties and drastic changes in physical properties after plastic working at room temperature. These alloys simultaneously offer super elasticity, super strength, super cold-workability, and Invar and Elinvar properties. The alloys consist of Group IVa and Va elements and oxygen and share the following three electronic magic numbers: (i) a compositional average valence electron number [electron/atom (e/a) ratio] of about 4.24; (ii) a bond order (Bo value) of about 2.87 based on the DV-Xα cluster method, which represents the bonding strength (*1*–*3*); and (iii) a "d" electron-orbital energy level (Md value) of about 2.45 eV, representing electronegativity. The properties emerge only when all three of these magic numbers are satisfied simultaneously. Various alloy composition combinations meet these criteria, such as Ti-12Ta-9Nb-3V-6Zr-O and Ti-23Nb-0.7Ta-2Zr-O [mole percent (mol %)], wherein each alloy has a simple body-centered cubic (bcc) crystal structure. In order to exhibit these properties, each alloy system requires substantial cold working and the presence of a certain amount of oxygen, restricted to an oxygen concentration of 0.7 to 3.0 mol %.

Typical properties of the alloys are shown in Fig. 1 for samples before and after cold swaging with 90% reduction in area (*4*). Tensile stress-strain curves shown in Fig. 1A indicate that cold working substantially decreases the elastic modulus and increases the yield strength and confirm nonlinearity in the elastic range, with the gradient of each curve decreasing continuously to about 1/3 its original value near the elastic limit. As a result of this decrease in elastic modulus and nonlinearity, elastic deformability after cold working reaches 2.5%, which is at least double the value before cold working. Generally, large elastic deformations that occur in so-called "super-elastic alloys" are known to be reversible martensitic transformations resulting from deformation, dubbed "pseudo-elastic deformation" (*5*, *6*). Conversely, the large elastic deformation in the alloy studied is an intrinsically different "true-elastic deformation," which is not accompanied by phase transformation. The elastic deformability of the cold-worked material has been found to increase with decreasing temperature, exceeding 4% at 77 K. The strength of the alloy increases with decreasing temperature, as in normal metals, reaching 1800 MPa at 77 K. Conversely, the elastic modulus of non-cold-worked samples increases with decreasing temperature, in the same manner as for normal metals, but, as shown in Fig. 1B, the elastic modulus of the cold-worked alloy remains about constant between 77 and 500 K. Elinvar alloys (*7*), which maintain a constant elastic modulus over a limited temperature range, have already been known. However, none of them has been known to maintain a constant elastic modulus over such a wide temperature range. Figure 1C shows the temperature dependence of linear expansion. In an annealed state, the alloy exhibits almost linear thermal expansion behavior similar to that of a normal metal and continues to expand with increasing temperature. Its linear expansion coefficient is about 8×10^{-6} K^{-1}. For the cold-worked alloy, the linear expansion coefficient does not exceed

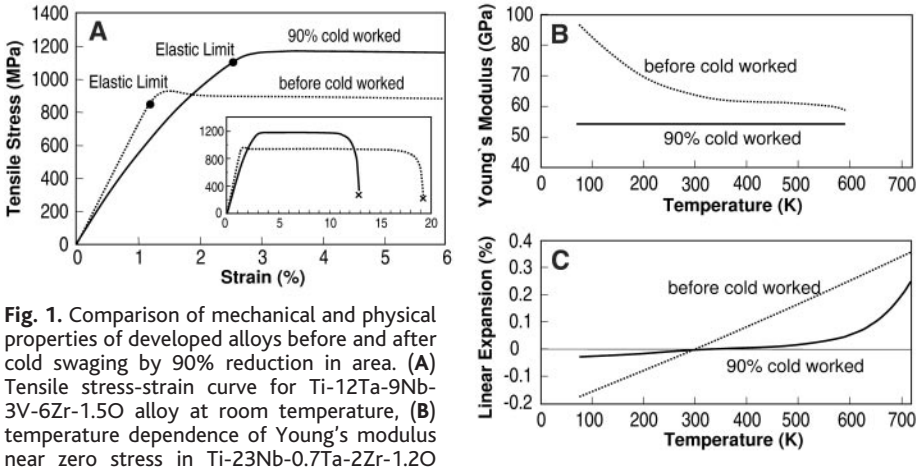

Fig. 1. Comparison of mechanical and physical properties of developed alloys before and after cold swaging by 90% reduction in area. (**A**) Tensile stress-strain curve for Ti-12Ta-9Nb-3V-6Zr-1.5O alloy at room temperature, (**B**) temperature dependence of Young's modulus near zero stress in Ti-23Nb-0.7Ta-2Zr-1.2O alloy, and (**C**) temperature dependence of linear expansion in Ti-23Nb-0.7Ta-2Zr-1.2O alloy.

[1]Toyota Central Research and Development Laboratories, Incorporated, Nagakute Aichi, 480-1192 Japan. [2]Institute of Engineering Innovation, University of Tokyo, Hongo, Bunkyo-ku, Tokyo, 113-8656 Japan. [3]Graduate School of Frontier Sciences, University of Tokyo, Hongo, Bunkyo-ku, Tokyo, 113-0033 Japan.

*To whom correspondence should be addressed. E-mail: saito@mosk.tytlabs.co.jp

2×10^{-6} K^{-1} over a temperature range of 100 to 500 K but shows a dramatic increase from about 600 K. The cold-worked alloy exhibits the Invar property over a wider temperature range than do conventional Invar alloys (*7*–*9*). A similar abnormality in thermal expansion behavior by cold working of shape memory alloys has recently been reported by Kainuma *et al*. (*10*). That phenomenon is caused by a reverse transformation of stress-induced martensite. Conversely, the abnormality in thermal expansion of the material investigated is completely unrelated to phase transformation. In many cases, Invar and Elinvar properties have traditionally been attributed to the magnetic moment of ferromagnetic alloys. However, our alloy is neither ferromagnetic nor antiferromagnetic, but paramagnetic.

The combined properties of the cold-worked alloy may make it extremely useful. For example, low elastic modulus and high strength can make the alloy suitable for ultralightweight springs, and its invariable elastic modulus and thermal expansion properties may make the alloy an ideal material for precision instruments for use in rugged environments such as in outer space.

The unusual physical properties shown in Fig. 1 suggest that the plastic deformation induced by cold working is of a considerably different nature from that of normal metals. This is supported by the observation of room-temperature super plasticity such that no amount of plastic deformation causes work hardening or a drop in ductility (fig. S1). Although the cold-worked material has a trivial uniform tensile elongation as seen in Fig. 1A, it shows a large local elongation (reduction in area) and an amazing capacity for compressive deformation, like that of clay, by virtue of its strange work-softening characteristics.

A typical microstructure of Ti-23Nb-0.7Ta-2Zr-1.2O alloy is shown in Fig. 2. An optical microstructure comparison of the annealed (Fig. 2A) and the cold-worked (Fig. 2B) materials indicates that the equiaxed beta grain microstructure of the annealed material changes into the characteristic "marble-like" structure after cold working. The marble-like structure appears to consist of assemblies of fine filamentary structures. A high-magnification transmission electron microscope (TEM) image of the cold-worked alloy shows local disturbances (bending) in the crystal lattice (Fig. 2C). The distribution of discrete 2- to 3-nm order strain contours is found to correspond to disturbances in the crystal lattice. However, observations at different magnifications and orientations revealed virtually no dislocations (fig. S2). In addition to exhibiting this nanoscale bending, the crystal lattice was found to bow at a radius of about 500 nm and at a scale of several tens of micrometers.

The following model testing was conducted in order to analyze the plastic deformation mechanism in detail. A microspecimen of annealed alloy having a parallel portion about 30 micrometers thick and 150 micrometers long was subjected to tensile testing under a microscope. Figure 3, A to D, shows the changes in the sample surface with the progress of tensile deformation. The sample surface exhibited no change through the initial deformation of about 3%, and subsequently a large line pattern suddenly appeared across the parallel portion. The number of line patterns increased intermittently as the strain increased. Figure 3E shows TEM images of thin films prepared with the use of the focused ion beam method of sections parallel to the tension direction and perpendicular to the surface of the specimen after the sample had undergone 10% tensile strain. The observed structures show that (i) the line patterns appearing at the sample surface are each "giant faults" having height differences of about 300 to 500 nm that appeared within an extremely short time; (ii) the faults formed

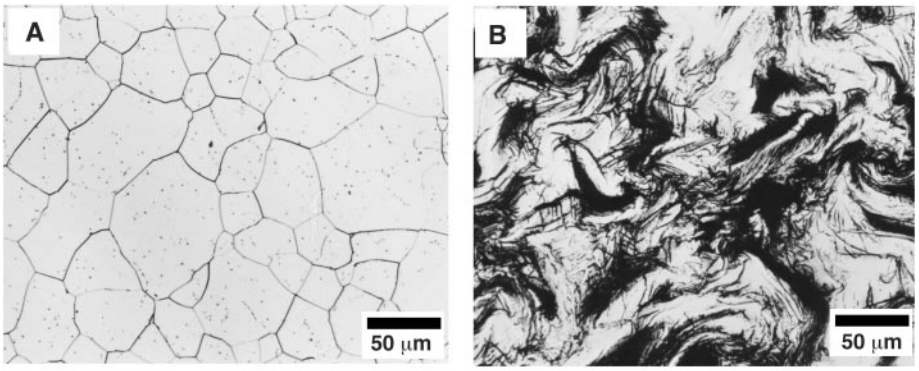

Fig. 2. Comparison of optical microstructure of Ti-23Nb-0.7Ta-2Zr-1.2O alloy (**A**) annealed at 1273 K and (**B**) cold-worked by 90% reduction in area. (**C**) A high-magnification TEM image of the cold-worked specimen with (110) normal incident beam using an ultrahigh voltage (1.2 MV) TEM. Local disturbances in the crystal lattice are indicated within open circles.

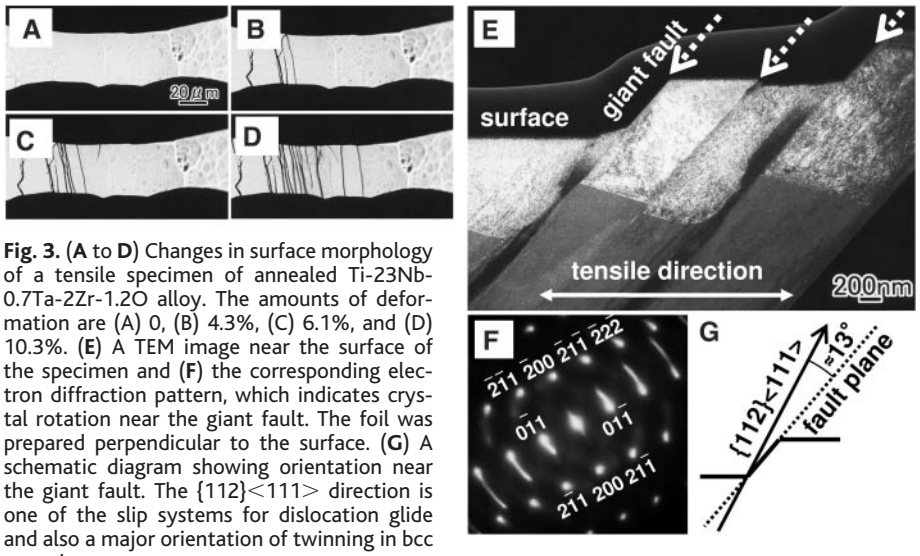

Fig. 3. (**A** to **D**) Changes in surface morphology of a tensile specimen of annealed Ti-23Nb-0.7Ta-2Zr-1.2O alloy. The amounts of deformation are (A) 0, (B) 4.3%, (C) 6.1%, and (D) 10.3%. (**E**) A TEM image near the surface of the specimen and (**F**) the corresponding electron diffraction pattern, which indicates crystal rotation near the giant fault. The foil was prepared perpendicular to the surface. (**G**) A schematic diagram showing orientation near the giant fault. The {112}<111> direction is one of the slip systems for dislocation glide and also a major orientation of twinning in bcc crystals.

along the plane of maximum shear stress at about 45° to the tensile direction, not on the possible bcc crystal slip planes or twin planes (Fig. 3G); (iii) the grain boundary is greatly curved near the faults, resulting in large elastic deformation; and (iv) highly distorted and localized strain fields were generated along the fault plane (Fig. 3F). This suggests that the plastic deformation mechanism of this alloy is an extremely large-scale and discontinuous phenomenon in which the deformation progresses by formation of giant faults. Thus, the marbled structure seen in Fig. 2B is thought to be developed by aggregation of the "giant faults," which was highlighted by chemical etching that reveals the strain field near the fault. Recrystallized grains nucleate along the filament structures upon reheating of the cold-worked material (fig. S3), supporting the view that the line pattern reflects the elastic strain field.

We examined the effect of cold working and the role of oxygen with ultrahigh-intense x-ray diffraction (XRD), electron energy loss spectroscopy (EELS) (*11*), and extended x-ray absorption fine structure (EXAFS) (*12*) using an 8-GeV synchrotron radiation beam (*13*). The XRD analysis revealed that the material is essentially composed of bcc phase at the cold-worked condition and that no phase transformation such as α" martensitic transformation occurs. The EELS analysis on the cold-worked specimen (Fig. 4A) revealed that the zero-loss image indicates the strain distribution. The flecked contrast at a scale of several nanometers observed in the TEM image was thus found to represent the elastic strain field distribution. In addition, the distribution of alloying elements (in particular zirconium) matches the size of the strain contours. Figure 4B compares the Fourier transformed spectra calculated from the K-edge spectra for niobium and zirconium atoms (EXAFS analyses) conducted on six sample types for determining the oxygen concentration and the effect of cold working. The niobium atoms (and tantalum atoms) exhibit about identical spectra in all six samples, whereas the zirconium atoms show obvious sample-to-sample differences. That is, (i) oxygen content and cold working produce no changes around Group Va elements, such as niobium and tantalum; (ii) oxygen atoms tend to build up around the zirconium atoms to form atom clusters; (iii) cold working equalizes the mean distance between the zirconium atoms and the surrounding first and second nearest substitutional atoms (mainly titanium); and (iv) cold working rearranges the oxygen atoms surrounding zirconium atoms.

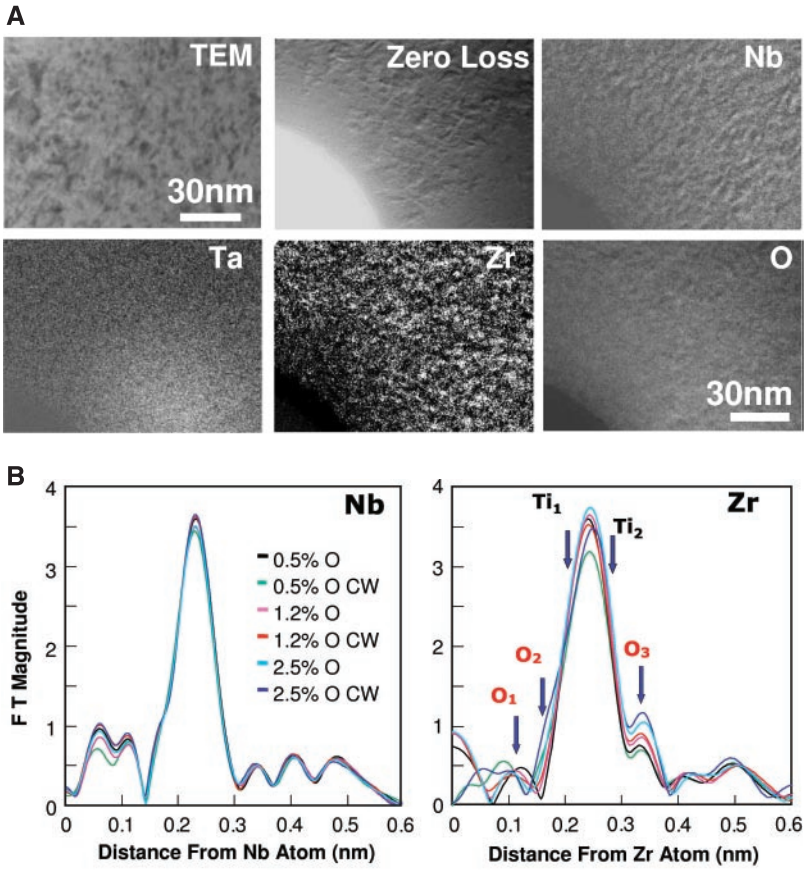

Fig. 4. (**A**) A distribution of alloying elements in the 90% cold-worked Ti-23Nb-0.7Ta-2Zr-1.2O alloy by EELS using a 200-kV TEM and a TEM image of the same magnification. (**B**) Comparison of the Fourier transferred spectra calculated from the K-edge EXAFS spectra for niobium and zirconium atoms using 8-GeV synchrotron radiation beam obtained for six sample types. Specimens of three oxygen levels of 0.5, 1.2, and 2.5 mol % were examined before and after 90% cold swaging. Ti_n and O_n represent positions of neighboring titanium and interstitial oxygen atoms, respectively. Strong dependences on both oxygen concentration and cold working are seen only for zirconium atoms, whereas the spectra around niobium atoms (same for tantalum atoms) are almost overlapping for all specimens.

Finally, we consider why only alloys of specific compositions exhibit the curious plastic deformation behavior. The Young's modulus of a Ti-X binary alloy system, comprising titanium and a Group Va element X (such as tantalum, niobium, or vanadium), was estimated from the first principles on the basis of the ultrasoft pseudopotential method (*14*, *15*) within generalized gradient approximation to the density function theory (*16*, *17*). The calculation showed an extremely low elastic modulus at a valence electron number close to that of the developed alloy (e/a = 4.24) and showed that the elastic constants c_{11} and c_{12} are nearly equal for this composition (fig. S4). In other words, the Young's modulus (E) approaches zero in the bcc crystal <100> direction, and the shear modulus (G) approaches zero in the <111> direction on the {011}, {112}, and {123} planes, a typical slip system in bcc metals (table S1).

Now we can deduce the plastic behavior of the alloy from the elastic properties described above. The value of the "ideal shear stress" has been estimated as about $0.11G_{111}$ (*18*) for bcc metals; such values for conventional metals are several dozen times the actual strength, whereas that for the developed alloy is estimated to be so small as to be comparable to the actual strength by virtue of the peculiar elastic anisotropy described above. Although in conventional bcc metals slip occurs as a result of shear deformation in the <111> closed packed direction on the {011}, {112}, and {123} slip planes, elastic deformation occurs readily in the developed alloy by virtue of its extremely small G value in this direction. Eventually, when local stresses reach their critical value (ideal shear stress) (*18*), shear deformation proceeds along the maximum shear stress plane without the aid of any dislocations. Here we should recall that the abnormal plastic deformation behavior of a Ti-X alloy of about a specific composition only appears upon addition of a certain amount of zirconium and oxygen. It may be possible that the Zr-O atom clusters, which distributed densely over an extremely short range, could effectively inhibit dislocation activity.

As a result, dislocation-free plastic deformation can be realized, and the "giant fault" visible in Fig. 3E dominates the plastic deformation. Such plastic deformation mechanisms unaccompanied by dislocation activity are thought to be the reason why huge plastic deformation is possible, as in the case of clay, and why no work hardening is exhibited. The formation of

"giant faults" does not lead to total failure, because the displacement equivalent to the fault formation is complemented by elastic deformations around the fault as seen in Fig. 3F. Therefore, as plastic working proceeds, elastic strain energy is accumulated. The accumulation of the elastic strain energy is accompanied by the coordinated displacement of the zirconium and oxygen atoms as shown in Fig. 4. The nanometer-scale bending is discrete and accumulates into large crystal curvatures of a scale of several tens of micrometers, which indicate that the large elastic strain energy is accumulated discretely and hierarchically in the alloy. We conceive, for the time being, that all the dramatic changes in physical properties by cold working seen in Fig. 1 are attributed to this accumulated nanoscale discrete elastic strain energy.

References and Notes

1. J. C. Slater, *The Calculation of Molecular Orbitals* (Wiley, New York, 1979).
2. F. W. Averill, D. E. Ellis, *J. Chem. Phys.* **59**, 6412 (1973).
3. M. Morinaga, N. Yukawa, T. Maya, K. Sone, H. Adachi, in *Sixth World Conference on Titanium*, Societé Française de Metallurgie et des Materiaux, Cannes, France, 6 to 9 June 1988, P. Lacombe, R. Tricot, G. Beranger, Eds. (Les Editions de Physique, Les Ulis Cedex, France, 1989), pp. 1373–1379.
4. Materials and methods are available as supporting material on *Science* Online.
5. T. W. Duerig, A. R. Pelton, in *Materials Properties Handbook: Titanium Alloys*, R. Boyer, G. Welsch, E. W. Collings, Eds. (American Society for Metals International, Materials Park, OH, 1994), pp. 1035–1048.
6. C. Baker, *Metal Sci. J.* **5**, 92 (1971).
7. Y. Nakamura, *IEEE Trans. Magn.* **12**, 278 (1976).
8. E. P. Wohlfarth, *IEEE Trans. Magn.* **11**, 1638 (1975).
9. C. E. Guillaume, *Proc. Phys. Soc. London* **32**, 374 (1920).
10. R. Kainuma, J. J. Wang, T. Omori, Y. Sutou, K. Ishida, *Appl. Phys. Lett.* **80**, 4348 (2002).
11. R. F. Egerton, *Electron Energy-Loss Spectroscopy in the Electron Microscope* (Plenum, New York, 1986).
12. B. K. Teo, *EXAFS: Basic Principles and Data Analysis* (Springer-Verlag, Berlin, 1986).
13. H. Kitamura, *J. Synchrotron Radiat.* **5**, 184 (1998).
14. D. Vanderbilt, *Phys. Rev. B* **41**, 7892 (1990).
15. K. Laasonen, A. Pasquarello, R. Car, C. Lee, D. Vanderbilt, *Phys. Rev. B* **47**, 10142 (1993).
16. P. Hohenberg, W. Kohn, *Phys. Rev.* **136**, B864 (1964).
17. W. Kohn, L. J. Sham, *Phys. Rev.* **140**, A1133 (1965).
18. C. R. Krenn, D. Roundy, J. W. Morris Jr., M. L. Cohen, *Mater. Sci. Eng. A* **319–321**, 111 (2001).

Supporting Online Material

www.sciencemag.org/cgi/content/full/300/5618/464/DC1
Materials and Methods
Figs. S1 to S4
Table S1

30 December 2002; accepted 4 March 2003

Packing C_{60} in Boron Nitride Nanotubes

W. Mickelson, S. Aloni, Wei-Qiang Han, John Cumings, A. Zettl*

We have created insulated C_{60} nanowire by packing C_{60} molecules into the interior of insulating boron nitride nanotubes (BNNTs). For small-diameter BNNTs, the wire consists of a linear chain of C_{60} molecules. With increasing BNNT inner diameter, unusual C_{60} stacking configurations are obtained (including helical, hollow core, and incommensurate) that are unknown for bulk or thin-film forms of C_{60}. C_{60} in BNNTs thus presents a model system for studying the properties of dimensionally constrained "silo" crystal structures. For the linear-chain case, we have fused the C_{60} molecules to form a single-walled carbon nanotube inside the insulating BNNT.

Crystal structure is key in determining the mechanical, electronic, thermal, and magnetic properties of materials. Silicon, for example, is a modest bandgap semiconductor in its common diamond structure, but in its high-pressure simple hexagonal structure it is a metal and a superconductor (*1*). In low-dimensional nanostructures, crystal structure conspires with additional quantum mechanical confinement and surface effects to dictate the (often unusual) material properties. Of current interest is the ability to reliably manipulate atomic or molecular species into different nanoscale configurations, in which the crystal structure is dictated not only by interatomic or intermolecular interactions but also by self-imposed surface energy terms (such as in suspended metal nanowires) (*2*, *3*) or externally applied geometrical constraints [(with examples ranging from liquids freezing in confined geometries (*4*) to atoms assembled on surfaces (*5*)]. Because of its high symmetry and relatively weak intermolecular interactions, the fullerene C_{60} presents a near-ideal system for studying different crystal structures possible in a weakly interacting, dimensionally constrained system.

We here report unusual nanowire crystal structures of C_{60} obtained by packing the spherical fullerene molecules into the interior spaces of boron nitride nanotubes (BNNTs). BNNTs (*6–10*) have an energy gap of 5 eV independent of wall number, diameter, or chirality and thus constitute desirable insulating structures for geometrically and electronically confining atomic, molecular, or nanocrystalline species. We find that filling small-diameter BNNTs results in a linear chain of C_{60} molecules, analogous to previously observed carbon nanotube "peapods" (*11*), but with a significantly smaller C_{60}-C_{60} intermolecular distance. With increasing BNNT inner diameter, new stacking configurations are obtained that are unknown for bulk or thin-film forms of C_{60}. Our results are well accounted for by a simple geometrical model of hard spheres packed within a cylindrical cavity. Through postsynthesis treatment, it is possible to fuse the C_{60} molecules together into carbon nanotubes, yielding as a final product single-walled carbon nanotubes individually sheathed within electrically insulating BNNTs.

Pure BNNTs were first synthesized with either a plasma-arc discharge method (*9*), yielding primarily double-walled BNNTs, or a carbon-nanotube substitution reaction (*10*), yielding multiwalled BNNTs. The as-synthesized nanotube-rich soot was heat treated in air at 800°C for 20 min to remove excess boron nanoparticles and to open the tips of the BNNTs. The gray, heat-treated tubes were then sealed in an evacuated (10^{-6} torr) quartz ampoule together with commercially obtained C_{60} powder (MER Corp., Tucson, Arizona, 99.5%) in about a 5:1 C_{60}:BNNT mass ratio and uniformly heated to between 550° and 630°C for 24 to 48 hours. The ampoules were broken open, and the resultant black material was sonicated in either isopropanol or chloroform and deposited onto lacey-carbon grids for transmission electron microscope (TEM) characterization, with TOPCON 002B, Phillips CM200, and JEOL 2011 microscopes operating at electron energies typically near 100 keV.

Figure 1 shows TEM images of BNNTs treated with C_{60}. In Fig. 1A, two double-walled BNNTs are shown. The upper of the two tubes in Fig. 1A has an inner diameter of ~1.3 nm. The interior of this tube is well resolved and shows a linear chain of nearly evenly spaced C_{60} molecules. This hybrid structure is very similar in appearance to previously reported (*11*) single-walled carbon nanotube/C_{60} peapods. The lower BNNT in Fig. 1A is partially filled with amorphous boron nitride; this filling has substantially prevented C_{60} infiltration. Figure 1B shows additional TEM images of BNNTs treated with C_{60}. The lower half of the figure shows a five-walled BNNT with innermost diameter of 1.3 nm, which is efficiently filled with a linear chain of C_{60}.

Department of Physics, University of California at Berkeley, Berkeley, CA 94720, USA. Materials Sciences Division, Lawrence Berkeley National Laboratory, Berkeley, CA 94720, USA.

*To whom correspondence should be addressed. E-mail: azettl@socrates.berkeley.edu